Available online at www.sciencedirect.com

ScienceDirect

Ceramics International 40 (2014) 9327–9335

CERAMICS INTERNATIONAL

www.elsevier.com/locate/ceramint

Investigation of yttria-doped alumina nanocomposites reinforced by multi-walled carbon nanotubes

Iftikhar Ahmad[a,*], Mohammad Islam[a], Abdulhakim A. Almajid[b], Bahareh Yazdani[c], Yanqiu Zhu[c]

[a]Center of Excellence for Research in Engineering Materials, Advanced Manufacturing Institute, King Saud University, P.O. Box. 800, Riyadh 11421, Kingdom of Saudi Arabia

[b]Department of Mechanical Engineering, College of Engineering, King Saud University, P.O. Box. 800, Riyadh 11421, Kingdom of Saudi Arabia

[c]College of Engineering, Mathematics and Physical Sciences, University of Exeter, Exeter EX4 4QF, United Kingdom

Received 29 November 2013; received in revised form 30 January 2014; accepted 30 January 2014
Available online 8 February 2014

Abstract

Nanocomposites of Y_2O_3 doped Al_2O_3 reinforced with 2 wt% MWCNTs were fabricated by hot-pressing. The influence of a small Y_2O_3 addition (300 ppm) on the microstructure and mechanical properties of CNT-reinforced Al_2O_3 was investigated. The resulting Y_2O_3 doped Al_2O_3-CNT nanocomposites showed near theoretical densities (> 99%) with an astounding 5 times finer grain size and substantial improvements in the fracture toughness (40%), flexural strength (20%) and hardness (18%) than pure Al_2O_3, prepared under identical experimental conditions. The Y_2O_3 addition improved the density of the matrix, eliminated the residual flaws and formed YAG (yttrium–aluminium–garnet) particles at the grain boundaries in the nanocomposites. The submicron YAG particles, together with the CNTs, promoted the Al_2O_3 matrix to form fine-grained microstructures and altered the fracture mode, thus leading to higher toughness and other mechanical properties. The improved mechanical properties allows for the Y_2O_3 doped Al_2O_3-CNT nanocomposites to be used for applications in load bearing structures.

Keywords: B. Nanocomposites; C. Mechanical properties; C. Toughness and toughening; Microstructure

1. Introduction

Among structural ceramics, alumina (Al_2O_3) is appreciated for high stiffness, excellent thermal stability and relatively low density, but its extreme brittleness restricts this promising ceramic from many advanced structural applications, such as in military armour systems, as aircraft engine parts and in space engineering [1–6]. In order to overcome the brittleness issue, carbon nanotubes (CNTs) with extremely high strength and exceptional flexibility have inspired researchers to investigate the possibility of incorporating them into Al_2O_3. Several reports on the CNTs-reinforced Al_2O_3 have demonstrated large enhancements in fracture toughness, hardness and other mechanical properties [7–13]. After years of rigorous research, the role of CNTs in Al_2O_3 ceramics has been well-documented, such as hampering the densification process, refining the matrix by grain pinning, increasing the fracture toughness by crack bridging/crack deflection, improving the wear resistance by sliding/rolling, and improving the electrical/thermal properties [2–15]. In literatures, issues such as the homogenous dispersion of CNTs, achieving higher densities of the nanocomposites, understanding the toughening mechanism and Al_2O_3-CNT interfacial bonding have been intensively discussed, whilst the microstructural tuning is hardly attempted [7–15]. Tailoring the microstructures of pure Al_2O_3 and Al_2O_3 based matrices with metal oxide (MgO, Ce_2O_3, Li_2O, Y_2O_3) has been an eminent practice [16–24]. For an example, the addition of a small amount of Y_2O_3 (< 1000 ppm) has upgraded the monolithic Al_2O_3 to a material with higher densities (99%), finer grains and higher mechanical properties. The role of Y_2O_3 in improving the densification, microstructures and mechanical properties of the ZrO_2-reinforced Al_2O_3 nanocomposites has been discussed

*Corresponding author. Tel.: +966 1 4699667; fax: +966 1 4670199.
E-mail address: ifahmad@ksu.edu.sa (I. Ahmad).

http://dx.doi.org/10.1016/j.ceramint.2014.01.156
0272-8842

[20–24]. Built on top of these successes, the study of potential advantages of Y_2O_3 in CNT-reinforced Al_2O_3 ceramics is thus an interesting subject.

This paper describes the fabrication and characterisation of Y_2O_3-doped Al_2O_3 matrix nanocomposites reinforced by CNTs, aiming to show the influence of a small amount of Y_2O_3 on the structure (densities, grain size, residual porosity), mechanical properties (fracture toughness, flexural strength, hardness) and the fracture mode of the Al_2O_3-CNT nanocomposites.

2. Experimental procedures

2.1. Materials and manufacturing process

Well-mixed powders of 300 ppm Y_2O_3 and pure Al_2O_3 reinforced with 2 wt% of CNTs were hot-pressed to fabricate the nanocomposites, as listed in Table 1. Fig. 1a shows the transmission electron microscopy (TEM) image of the multi-walled CNTs used in this study, supplied by Tsinghua University, Beijing, China, and the CNTs exhibited an average diameter $\varnothing < 40$ nm. We first suspended the CNTs into distilled water by adopting a colloidal chemistry technique, as described earlier [12]. Al_2O_3 nanoparticles having a mean particle diameter of ~40 nm (Sigma-Aldrich, UK) were separately suspended into distilled water with the aid of 60 min sonication, then the desired amounts of Y_2O_3 nanoparticles (∅25–30 nm, Sigma-Aldrich, UK) were slowly added to them. The suspension was sonicated for another 60 min, in order to obtain an even distribution for better results. Subsequently, the well-dispersed CNT/water suspension was poured into the Al_2O_3 and Y_2O_3 mixture water suspension, and the combined suspension was again sonicated for 120 min to assure a thorough mixing of the nanocomposite constituents. The mixture was dried at 130–150 °C to acquire well-mixed powders. A typical example of well-dispersed ceramic nanoparticles covering a single CNT, as revealed by TEM, is shown in Fig. 1b. The dry powders were then hot-pressed in the form of discs of ∅ 32 ± 0.5 and 3 ± 0.5 mm thick, at the University of Mining and Technology, Beijing, China. Hot-pressing was carried out at 1600 °C for 60 min, under a constant pressure of 40 MPa during the whole sintering process under vacuum of 6.2×10^{-2} Pa. Pure and Y_2O_3-doped Al_2O_3 reference samples, without CNTs, were also fabricated.

Table 1
Mechanical properties of Y_2O_3 doped CNT-reinforced Al_2O_3 nanocomposites.

Sample designation	Matrix material	CNT contents (wt%)	Y_2O_3 contents (ppm)	Vickers hardness (*HV*) GPa	Flexural strength (σy) MPa	Fracture toughness (K_{IC}) MPa $m^{1/2}$
A0	Al_2O_3	–	0	16.0 ± 0.3	357 ± 27	3.0 ± 0.2
A3Y	Al_2O_3	–	300	16.5 ± 0.2	359 ± 22	3.2 ± 0.3
A2C	Al_2O_3	2	0	18.2 ± 0.2	367 ± 18	4.3 ± 0.3
A2C3Y	Al_2O_3	2	300	19.4 ± 0.2	442 ± 15	5.0 ± 0.1

2.2. Density and structural characterisation

Apparent densities of all sintered samples were measured by the water buoyancy (Archimedes) method using distilled water. Prior to measurements, surface cleaning of all samples was performed by using fine SiC paper. Theoretical densities for Al_2O_3, Y_2O_3 and CNTs of 3.99 g/cm^3, 5.01 g/cm^3 and 1.85 g/cm^3 respectively, were used for relative densities calculations in this work [10,25].

Phases of sintered samples were acquired using a Cu K_α radiation from a X-ray diffraction machine (D8 Advanced X-ray Differactometer manufactured by Bruker Corporation), and were identified with the help of Bruker Advanced X-ray Solutions computer software. Fracture surfaces of selected samples were studied using a Philips/FEI scanning electron microscopy (SEM). For detailed grain boundaries study and accurate determination of the grain size, all solid samples were finely polished up to 1 μm and then thermally etched in a tube furnace under an Ar atmosphere at 1400 °C for 15 min. Prior to SEM observation, all samples were coated with a thin layer of Au. An interesting and convenient chemical etching technique was also adopted to prepare samples for TEM analyses. Before chemical etching, the solid nanocomposite sample was milled to fine size and immersed in NaOH solution for several weeks then rinsed repeatedly with distilled water. The residue was finally transferred to a carbon coated lacey copper grid for subsequent investigation using a JEOL 2000 FX TEM.

2.3. Mechanical properties evaluation

All sintered discs were sliced into rectangular bars of 25 ± 1.5 mm (length) × 2 ± 0.15 mm (breadth) × 2.5 ± 0.20 mm (height) using a diamond cutting disc, which were subjected to three-point bending test using a 20 mm bending span and 0.50 mm/min testing speed. Eq. (1) was used for the flexural strength (σ_f) assessment, where F is the load at the fracture point, L the span length, b the sample breath and d is the sample thickness [12].

$$\sigma_f = \frac{3FL}{2bd^2} \tag{1}$$

Small samples of 10 ± 1.0 (length) × 10 ± 1.0 (breadth) × 4 ± 0.25 (thickness) mm were also prepared for hardness evaluation. Prior to testing, all samples were cold mounted using epoxy resin, and then ground on diamond pads of 120 and 220 grit and polished to 6 μm and 1 μm by using DP-suspension on polishing cloths. 9.8 N loads for 15 s was selected on a M-400 hardness tester (LECO, Japan) for the microhardness testing and the Vickers hardness number (*HV*) were further converted to GPa [6]. Young's modulus of all samples was calculated by applying Eq. (2). In which E is Young's modulus, ρ is the bulk density of the sample, V_c is the compression velocity and V_s the shear velocity [26].

$$E = \frac{V_s{}^2\rho(3V_c^2 - 4V_s^2)}{V_c^2 - V_s^2} \tag{2}$$

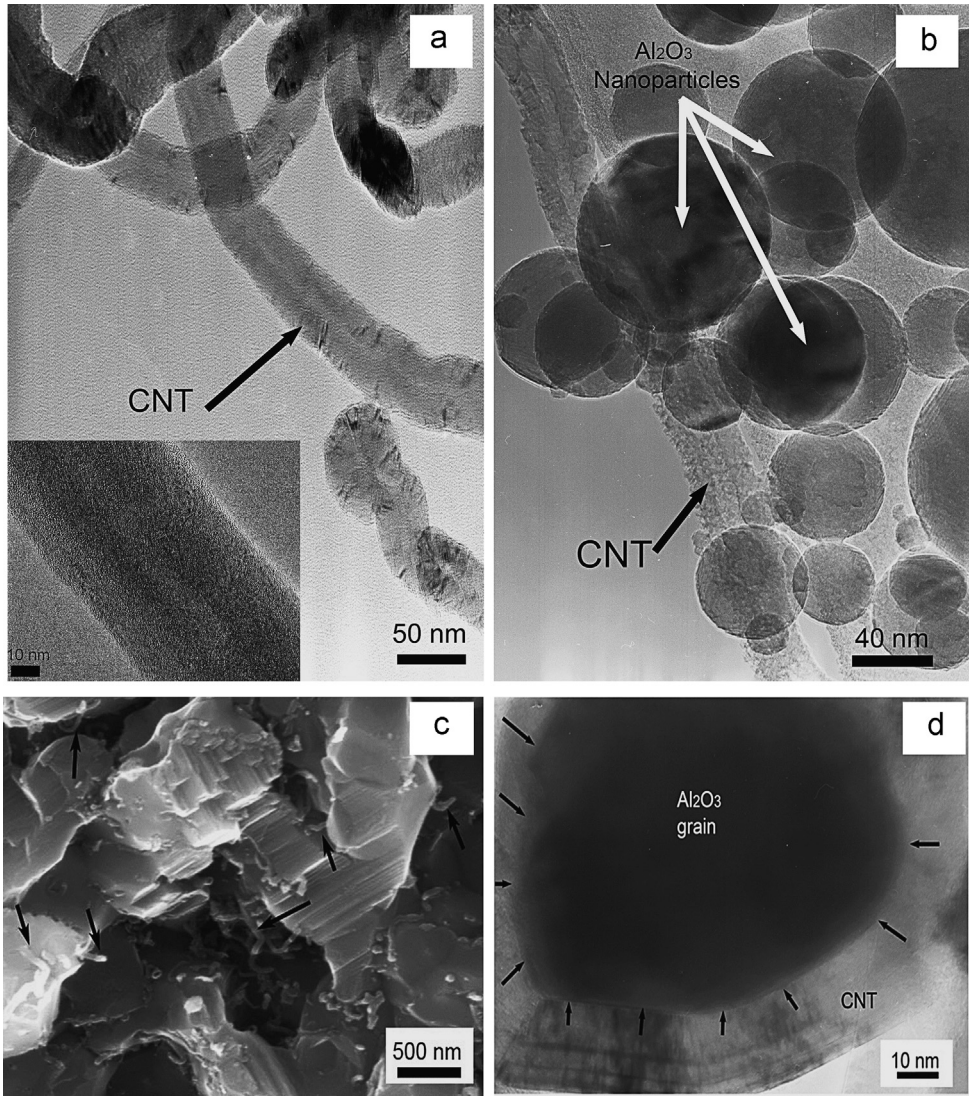

Fig. 1. TEM images of (a) pristine CNTs, (b) CNT/Al_2O_3 mixture, where a CNT (black arrow) is clearly visible within Al_2O_3 nanoparticles (white arrows), (c) Fractured surface SEM image showing individually dispersed CNTs in Al_2O_3 matrix (black arrows) and (d) high resolution TEM image shows CNT pinning the Al_2O_3 grain.

The time-of-flight velocities for both compression and shear wave propagation through the composite samples were determined by employing a ultrasonic pulse-echo technique. 20 MHz centre frequency, ∅ 6 mm contact TMP-3 transducer supplied by Sonatest, UK, was utilised for compression measurements, whereas 10 MHz centre frequency, ∅ 10 mm contact V221-BA transducer manufactured by Panametrics, USA, was used for the shear measurements. In all pulse echo measurements, suitable couplant materials were used in each case to ensure optimum contact between the samples and transducers. Indent crack measurement (ICM) method was also practiced in this case, only to provide a reference fracture toughness (K_{IC}) of samples, due to the increasing doubt on the reliability of this technique. For this purpose, length of cracks generated during indentation was carefully measured from the center by using scanning electron microscopy, (Philips/FEI XL30 FEG-ESEM), in combination with computer software ImageJ (Image Processing and Analysis in Java).

$$K_{IC} = 0.016\left(\frac{E}{H}\right)^{1/2}\left(\frac{P}{c^{3/2}}\right) \quad (3)$$

The fracture toughness was calculated by following Eq. (3), where E is Young's modulus, H is the hardness and c the radial crack length generated by Vickers's indentation [27].

3. Results and discussion

3.1. Physical properties and microstructure

SEM microstructure analysis of the fractured surface (Fig. 1c) indicated the success of the colloidal chemistry techniques adopted in this study [12]. It is found that uniformly dispersed individual CNTs (2 wt% addition) exist in the fractured Al_2O_3 matrix. Wrapping of individual CNTs around

growing Al_2O_3 grain boundaries, as evident in Fig. 1d, during the long hot-press sintering period, is another processing challenge. Although it hindered the coalescence of the matrix grains, resulting in fine grain size which is beneficial to the final properties, this hindering effect, at the same time, prevented the grains from sealing off the voids amongst them. Hence, the final sintered densities were lower in the Al_2O_3-CNT nanocomposites than that of the plain Al_2O_3, as displayed in Fig. 2 [8,28,29]. High magnification SEM microstructure images of the polished and thermally etched surfaces of the dopant-free nanocomposites (Fig. 3b) showed the presence of several flaws/porous features inside the matrix grains (black arrows). Presumably, the generation and detachment of these pores occurred as a result of grain boundary migration during the course of high pressure and high temperature consolidation process, which were subsequently trapped inside the grains, thus contributing to the decreased nanocomposite densities [30].

In case of CNT-reinforced nanocomposites with Y_2O_3 doping, the densities after consolidation nearly reached the theoretical values ($>99\%$), as graphically represented in Fig. 2. Several reports have stated that Y_2O_3 as a dopant has an imperative role in altering the grain boundary chemistry, lattice structure and surface diffusivity of Al_2O_3 matrix grains in the nanocomposites. These improved sintering ability arising from the control of grain boundary structure and pore mobility, leads to higher densities [30,31]. The SEM micrographs have clearly demonstrated the elimination of grain porosities due to Y_2O_3 doping, in both monolithic Al_2O_3 (Fig. 3c) and Al_2O_3-CNT nanocomposites (Fig. 3d). In this context, Fang et al. have previously suggested that Y_2O_3 doping serves two purposes, namely, (i) influencing the mass transport of the Al_2O_3 matrix grains by controlling the diffusion of Al and O ions and, (ii) hindering the detachment of pores from the grain boundaries during the migration, preventing them being trapped inside the matrix grains. The pores are thus eventually shifted to grain junctions during the last stage of sintering [18]. Based on these results, it is possible that the Y_2O_3 doping has efficiently contributed towards eradicating the porosity from the matrix grains, besides sealing the gaps at triple-grain junctions by segregating in the form of YAG particulates, thus leading to higher sintered densities for doped nanocomposites.

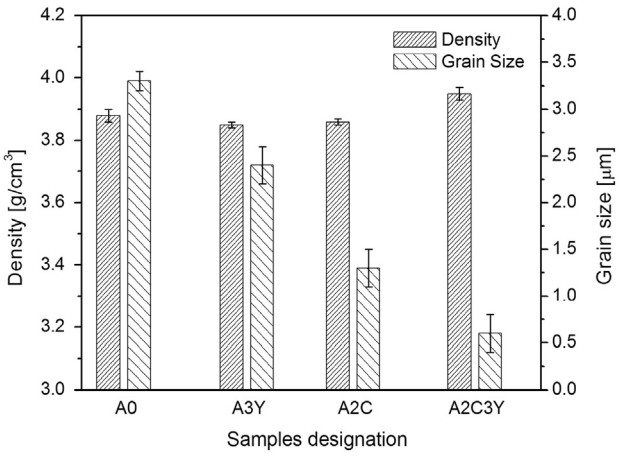

Fig. 2. Densities and grain size of monolithic Al_2O_3 and Al_2O_3-CNT nanocomposite samples with/without Y_2O_3 doping.

The solubility limit of Y_2O_3 in the Y_2O_3–Al_2O_3 system is 6–10 ppm. Hence, the excessive amount of Y_2O_3 generally segregates at the matrix grain junctions in the form of another phase [28,32]. This fact is corroborated by high magnification SEM images of the thermally etched samples of the doped Al_2O_3 and nanocomposites (Fig. 3e and f), in which the existence of particulate precipitates of another phase at junctions of the Al_2O_3 grain (indicated by white arrows) is clearly revealed. EDS analysis of the same particulate confirmed the presence of yttrium (Y) and oxygen (O) in both the doped Al_2O_3 and the doped nanocomposites (insets of Fig. 3e and f). XRD patterns of all the samples, shown in Fig. 4, were indexed for crystalline α-Al_2O_3 (JCPDS no. 01-078-2426) for the matrix phase, and $Y_3Al_5O_{12}$ (YAG) (JCPDS card no. 01-072-1853) which must be corresponding to the precipitates. The characteristic peaks of CNTs were absent in all nanocomposite samples due to their low content and possible overlap of the strongest (0 0 2) peak of CNTs (JCPDS no. 01-075-1621, included in Fig. 4 as a reference) with the (012) peak of Al_2O_3.

The presence of CNTs along Al_2O_3 grain boundaries leads to a 50% reduction in the grain sizes, by a grain impediment phenomenon, as graphically (Fig. 2) and structurally (Fig. 3a and b) represented. Moreover, the microstructure of dopant-free nanocomposites in Fig. 3b demonstrates the discrete fine and coarse grain areas (highlighted by black circle).These structural irregularities may be attributed to the hitches in achieving homogenous CNT distribution in Al_2O_3 matrix [9,11,12]. Several factors such as Van der Waals tube–tube attractions, fibrous morphology and high aspect ratio (length to diameter) could have promoted the CNT entanglements, thus controlling the ideal CNT concentrations level in the matrix to a certain limit (<2 wt%). Studies suggested that homogenous dispersion of CNTs below this concentration limit was attainable [8–12]. Taking into account the CNTs dispersion issue and the heterogeneous microstructures in Fig. 3b, we believe that CNTs may not be available at some Al_2O_3 grain boundaries to act as a pinning agent. Thus, the grain impediment role associated with CNTs does not seem to be prevalent in the entire microstructure of the nanocomposites.

Y_2O_3 doping in the same nanocomposites generated a fine-grained and homogenous microstructure, as demonstrated in Fig. 3d. A high magnification SEM image (Fig. 3f) of the thermally etched doped nanocomposite has provided useful topographic details that are helpful in understanding the exact role of the dopant in the microstructural improvements. Two important features were particularly noted in Fig. 3f, (i) bimodal grain size distribution representing relatively smaller YAG grains around large matrix grains and (ii) defect-free prominent matrix grain surfaces in Y_2O_3 doped nanocomposites that elucidate the excellent thermal stability of Al_2O_3. Contrary to the physical/mechanical dispersion of CNTs in the Al_2O_3 matrix, YAG precipitates are thermodynamically formed from Y_2O_3–Al_2O_3 solid solution

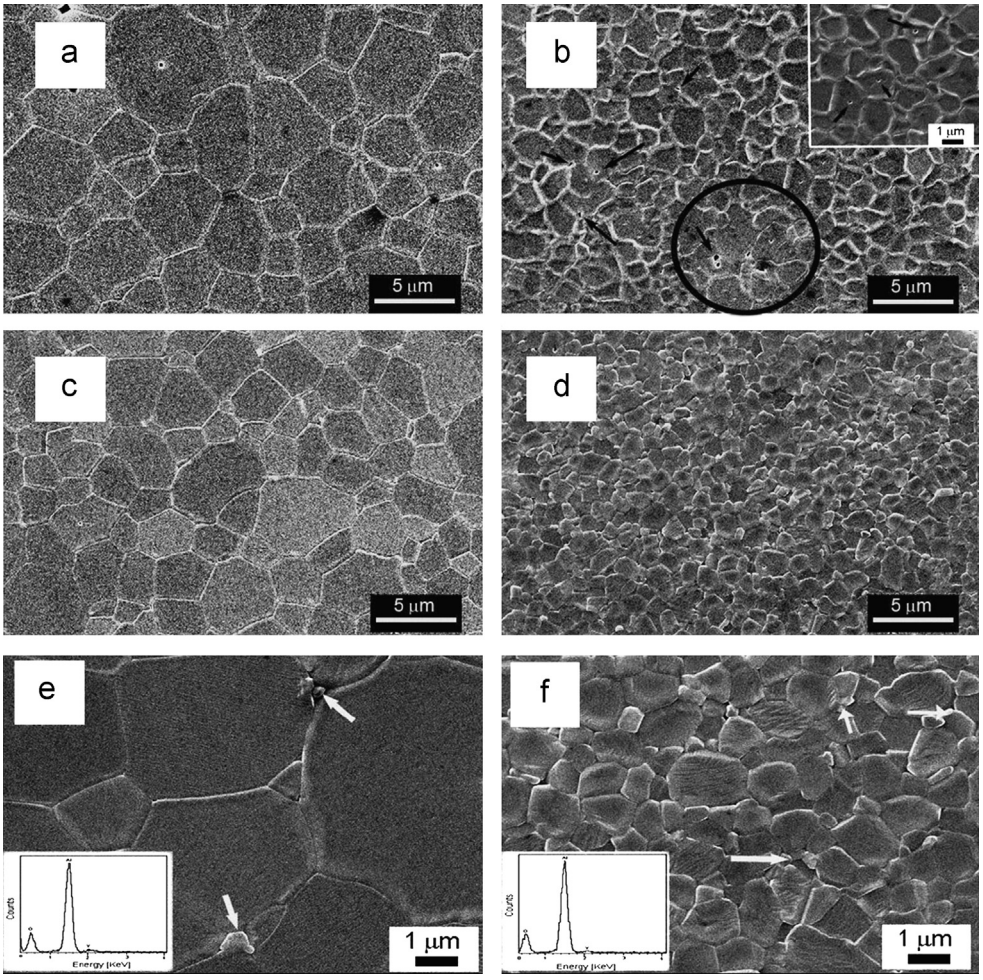

Fig. 3. SEM images of polished and thermally etched (a) monolithic Al_2O_3-coarse Al_2O_3 grains, (b) Y_2O_3-free nanocomposites, showing heterogeneous fine and coarse (black circle) grained microstructure with residual flaws/pores (black arrows) in inset, (c) Y_2O_3-doped Al_2O_3 showing equiaxed grains, (d) Y_2O_3-doped nanocomposites exhibit flaw-free, fine-grained and dense microstructure, (e) Y_2O_3-doped Al_2O_3 showing submicron $Y_3Al_5O_{12}$ precipitates (white arrow) at grain junctions with EDS analysis of the same precipitates in inset, and (f) Y_2O_3-doped nanocomposite showing $Y_3Al_5O_{12}$ precipitates (white arrow) within matrix grains, at high magnification with EDS analysis of precipitate particle in inset.

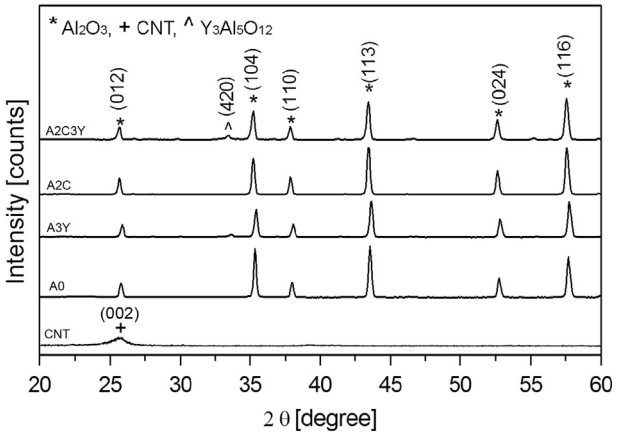

Fig. 4. XRD patterns of powdered CNTs and sintered samples of Al_2O_3 and Al_2O_3-CNT nanocomposites containing 0 ppm (A0, A2C) and 300 ppm (A3Y, A2C3Y) Y_2O_3, respectively.

through a phase-transformation process, thus their existence and thorough distributions in the overall microstructure are rational [31]. This leads to the advantages of potentially filling the voids otherwise existed at grain junctions for an enhanced densification. Simultaneously, they will also provide additional pinning sites in those regions of microstructures where there are no CNT presences (Fig. 3b–black circle). Numerical simulation has depicted that the effectiveness of grain pinning in polycrystalline materials largely depends on the end size (small particles are more effective than larger ones) of the precipitate particle [32,33]. In fact, topographic details of the doped nanocomposite samples (Fig. 3f) clearly showed the very fine feature of the YAG precipitates, exhibiting submicron dimensions around matrix grains. These results imply that, compared with pure Al_2O_3, the initial 50% grain size reduction in the dopant-free nanocomposites is purely due to CNT's grain pinning effect; however the further ~30% grain reduction in the doped nanocomposites is ascribed to the effect of Y_2O_3. Concisely, the Y_2O_3 dopant will contribute in a number of ways towards the quality improvement of CNT-reinforced Al_2O_3, including (i) the removal of sintering defects (porosity) which allowed the sintering pressures to consolidate further the matrix grains, (ii) substitution of the grain junction voids with submicron YAGs for enhanced densities, and (iii) provision of more grain

pinning sites to suppress the matrix grain coarsening through Zener pinning phenomenon [32]. The combined role of these phenomena eventually led the Y_2O_3 doped Al_2O_3-CNT nanocomposites to near theoretical densities and 5 times finer microstructures, compared to the pure Al_2O_3.

3.2. Mechanical properties and toughening mechanism

Indent crack method (*Chantikul* model) was adopted to assess the fracture toughness (K_{IC}) of all sintered samples in this study. Several empirical relationships based on indent crack lengths have been adopted to evaluate the K_{IC} of ceramic materials and each led to different results [6–13]. For example, most recently Sarkar et al. calculated the K_{IC} values of Al_2O_3-CNT nanocomposites by employing *Niihara* and *Liang* models and reported moderately related and sufficiently higher K_{IC} values, compared to the K_{IC} values of the same samples obtained by SENB (single edge notched beam) testing technique, respectively [34]. Inconsistent results have turned down the indent crack technique for the validation of engineering components especially for load bearing applications, however it is still widely employed for K_{IC} value comparisons [9,11,13,35]. The weak grain bonding, large grain sizes, residual flaws and intergranular fracture mode are generally attributed to the low fracture toughness/strength of monolithic Al_2O_3. Our hot-pressed plain Al_2O_3 samples also exhibited similar results (shown in Table 1), well in line with those literature reports [2–16].

A 30% higher K_{IC} value of the dopant-free nanocomposites, against the reference monolithic Al_2O_3 (indicated in Table 1), suggests that the CNTs have somehow transferred their strong and flexible feature to the matrix. Fig. 5 clearly shows firm attachment of numerous individually dispersed CNTs in the matrix, representing a strong CNT/Al_2O_3 bonding, as proposed by Ahmad et al. and Sarkar et al. in their separate reports [10,34]. Furthermore, CNTs bridged the cracking gaps (Fig. 5a, black circles and Fig. 5b, black arrow) and resulted in resistance to pullout (Fig. 5, white arrows), thus strengthened the composites and led to higher fracture toughness. On top of the influence of CNTs on toughness enhancements, a negligible (3%) improvements in the flexural strength of Al_2O_3-CNT nanocomposites than monolithic Al_2O_3 was attained. Although Fig. 6b clearly showed the transgranular fracture mode (operates when the grain boundary attained the fracture strength near the matrix grain) in Al_2O_3-CNT nanocomposites, however the presence of residual flaws in the microstructure of nanocomposites elucidated the low fracture resistance [36]. The sensitivity of residual flaws in ceramics can be gauged by an empirical square root relationship ($\sigma_F \infty l^{-0.5}$) which describes the fracture strength (σ_F) dependency on the flaw (c), where (c) is calculated with the grain size (l) [37,38]. Moreover, the flaw morphology and their high population might have other influences in lowering the amounts of stress required to initiate a crack. For example, sharp flaws (Fig. 6b, white circle) are logically more susceptible to stress concentration than blunt ones (Fig. 6b, white square). Based on these topographic details, it is predicted that

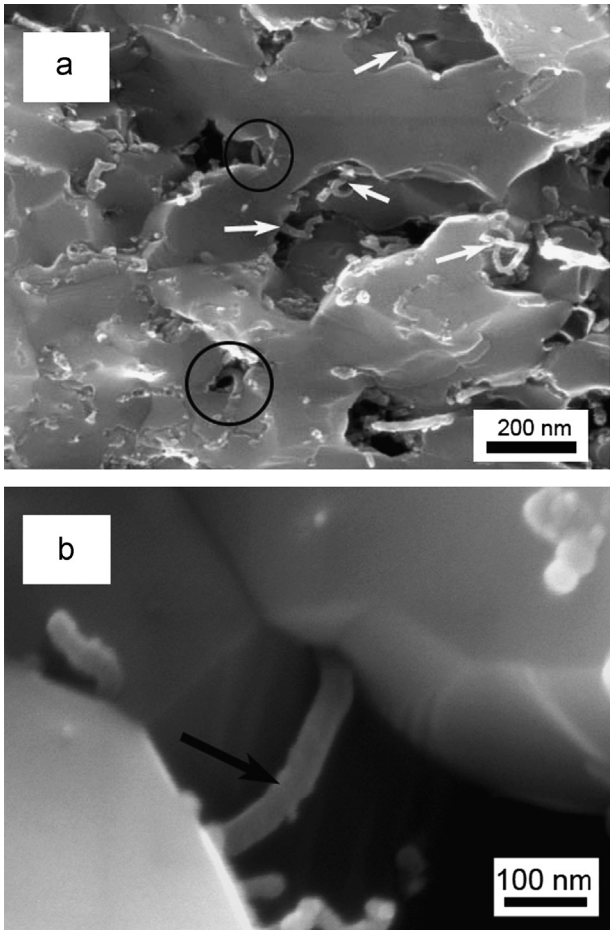

Fig. 5. SEM images. (a) The fractured surface of Al_2O_3-CNT nanocomposites, exhibiting CNTs across the flaws (black circles), CNT pull-out (white arrows) and (b) CNT bridging the crack surfaces (black arrow).

the failure in Al_2O_3-CNT nanocomposites probably started on piling a large amount of stresses around the flaws. Upon tensile loading, fractures occur instantaneously at the flaw's edge, rather than through intergranular, which normally occurs along weakly bonded matrix grain boundaries. Though CNTs were indeed observed inside these flaws (pointed with white arrows in Fig. 6b), it is quite possible that they could not effectively reinforce the materials due to the weak bonding with their respective grains across these flaws, thus the failure started at much lower loads than expected. The transgranular fracture mode observed in the nanocomposites however depicts the strong bonding between matrix grains and CNTs, and the straight indent crack propagation profile confirms the existence of such a failure mechanism in the dopant-free nanocomposites, as shown in Fig. 7c. Hence, the failure in Al_2O_3-CNT nanocomposite is thought to occur mainly through transgranular fracture which led to the higher fracture toughness, rather than the mixed inter-trans granular mode, as proposed by other [34]. However, we believe that the residual flaws suppressed the CNT's strengthening role and hindered the Al_2O_3-CNT nanocomposites to gain maximum toughness and strength. Thus their elimination is imperative.

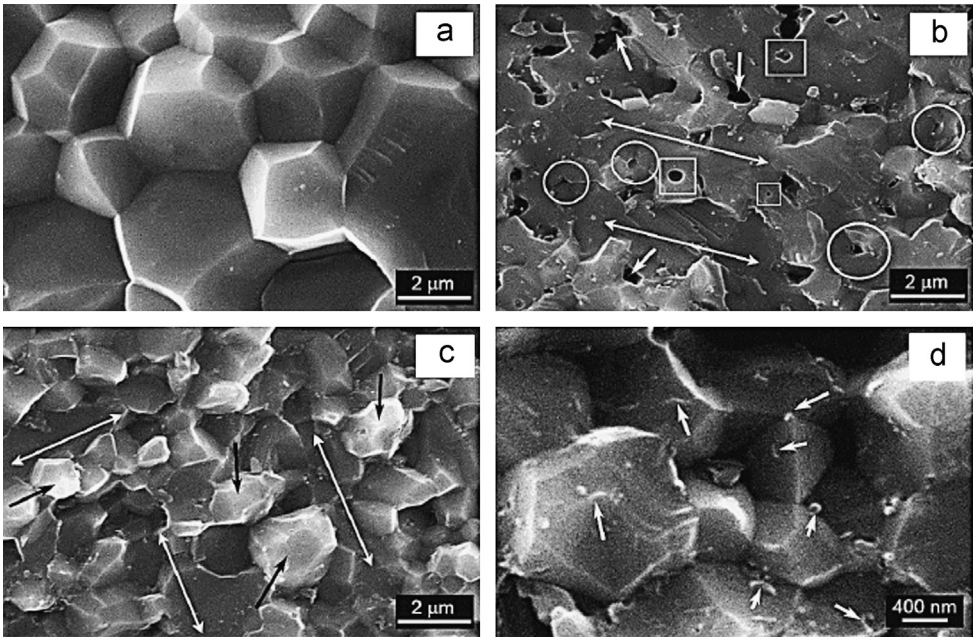

Fig. 6. SEM images of fractured surface: (a) monolithic Al_2O_3-large grains with intergranular fracture; (b) Y_2O_3-free nanocomposites showing residual porosity (white square), sharp flaws at matrix grain junctions (white circle), CNTs within flaw cavity (short white arrow), transgranular fracture (double-headed long white arrows); (c) mixed mode fracture in doped Al_2O_3-CNT nanocomposites-transgranular (double-headed long white arrows), intergranular (short black arrows); and (d) high-magnification SEM image of doped nanocomposites showing CNTs (short white arrows) at individual matrix grains.

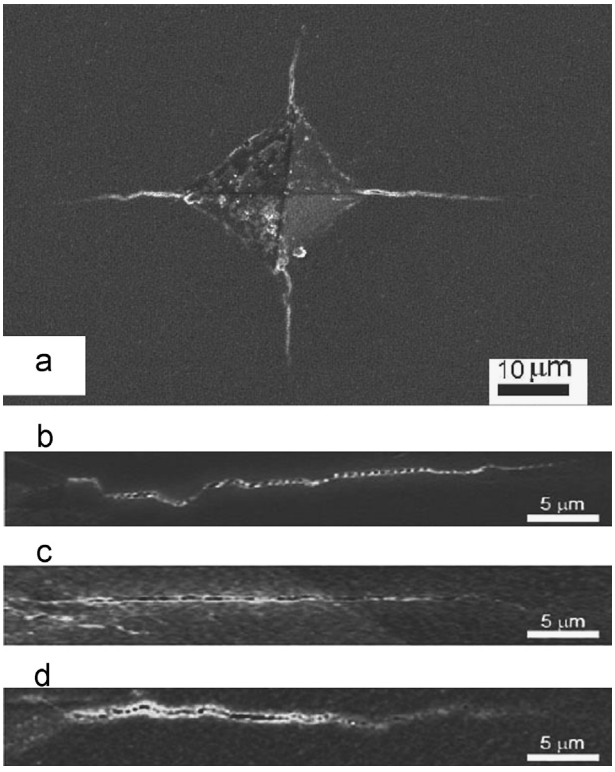

Fig. 7. SEM images of (a) Vickers's hardness indent at 9.8 N used for fracture toughness assessment and indent crack profile of (b) monolithic Al_2O_3, (c) dopant-free nanocomposites and (d) Y_2O_3 doped Al_2O_3-CNT nanocomposites.

Y_2O_3-doped nanocomposites demonstrated a 40%, 15% higher K_{CI}, and a 20%, 17% higher flexural strength (σ_f) than monolithic Al_2O_3 and dopants-free nanocomposite respectively, as summarised in Table 1. By comparing the fractographs, a distinctive fracture mode change from transgranular (Fig. 6b) in the dopant-free nanocomposites to a mixed inter-transgranular (Fig. 6c) in doped nanocomposites is clearly evident, without obvious flaws and other structural defects. As illustrated in previous section, the Y_2O_3 has improved the density, segregated at the grain boundaries and formed the YAG phase preferably at Al_2O_3 grain junctions in the doped nanocomposites, thus offering the two potential advantages, (a) residual flaws elimination and (b) grain size reduction. Furthermore, Takigawas et al. have suggested that a good contact between the YAG phase and Al_2O_3 could exist, hence a smooth transfer of dislocations (generated upon loading) from the matrix grains to bi-grain junctions through the YAG phase instead of piling up at triple-grain junctions may be deduced [39]. Deng et al. have also proposed that due to Y^{3+} ions segregation on the weak Al_2O_3–Al_2O_3 grain boundaries, an intergranular fracture mode was expected in the doped nanocomposites, otherwise a mixed inter-trans granular fracture mode was observed (Fig. 6c) [40]. Indeed, Fig. 7d shows a mixed indent crack profile in the doped nanocomposite which is neither zigzag nor straight, indicating the complexity of the fracture modes.

High-magnification SEM image of fractured surfaces of the doped nanocomposites has revealed that fewer CNTs are within individual matrix grains, and the composite underwent an intergranular fracture, as shown in Fig. 6d (white arrows). It is probably that in regions where less CNTs exist the matrix grains could not be properly reinforced, thus leading to the intergranular fracture. This phenomenon may be associated with deficient CNTs at individual grain level, and with the weak matrix grain boundaries due to dopant segregation. Despite these hurdles, the available CNTs, in both cases,

dissipated energy via elastic deformation and nanofriction through crack bridging and pull-out toughening mechanisms respectively, as reported by many groups [7–12,34]. The fine-grained structure in doped nanocomposites is beneficial to the increased critical strain-energy release rate, by providing more crack deflections during the intergranular fracture [40]. In this way, the mixed (inter and trans granular) fracture modes with the support of fine grains and flaw-free microstructure led the doped nanocomposites to a higher fracture toughness (15%) and flexural strength (17%) than the dopant-free counterparts.

The hardness of the monolithic Al_2O_3, dopant-free and doped nanocomposites was measured to be 16.0, 18.2 and 19.4 GPa, respectively. Usually, grain boundaries and reinforcing constituents are considered as pinning points in the matrix microstructures, as they impede the dislocation movements across their respective microstructures by hindering the onset of plasticity, thus making the fine-grained ceramics based composites harder [41,42]. Moreover, the Hall–Petch equation (Eq. 4) that was originally developed to predict the relationship between the yield strength and grain sizes of metallic materials has also been found equally suitable for assessing the hardness of ceramics [43].

$$H = H_R + Kd^{-1/2} \tag{4}$$

where H is the measured hardness by Vickers indentation, H_R is the reference hardness, K is the proportionality constant and d the mean grain size. The relationship between hardness and grain sizes is evident from Eq. 4. Hence, the 12% higher hardness in case of the dopant-free nanocomposites than pure Al_2O_3 is possibly due to the 50% finer grains and good CNT-matrix bonding [10,34]. The role of Y_2O_3 doping in the microstructure tuning in nanocomposite granted extra advantages, such as minimising the stress concentration sites (removal of residual flaws/pores), extra grain boundaries (grains refinement) and additional crack resistance through the mixed mode fracture mechanism (fracture-mode alteration), and all these resisted deformations, and consequently leading to a further 6% and 18% higher hardness than the dopant-free composites and the parental monolithic Al_2O_3, respectively.

4. Conclusions

A small amount of Y_2O_3 addition into the Al_2O_3 matrix refined the overall microstructure of the Al_2O_3-CNT nanocomposites and improved their key mechanical properties. The Y_2O_3 doping resulted in a near theoretical density of $>99\%$, which is attributed to the improved sinterability and the removal of residual flaws/pores within the matrix. A 80% reduction in the grain size in the doped Al_2O_3-CNT nanocomposites than the pure Al_2O_3 was due to the grain boundary pinning associated with both the CNTs and submicron YAG ($Y_3Al_5O_{12}$) participate particulates. Furthermore, the Y_2O_3 doping also contributed to the fracture mode transformation from the transgranular in dopant-free nanocomposites to a mixed inter-trans granular fracture mode in the doped nanocomposites. The fracture toughness, flexural strength and hardness values for Y_2O_3 doped Al_2O_3-CNT nanocomposites showed a respective percentage increase by 40, 20 and 18 than the pure Al_2O_3 samples, while an improvement of 15%, 17% and 6%, respectively, was achieved than the dopant-free nanocomposites. These results suggest that the microstructure refinement of the dopant, combined with the excellent strength of CNTs, have upgraded the Al_2O_3 to a mechanically superior nanocomposite that will be suitable for a diverse engineering application.

Acknowledgements

First author express sincere gratitude to the CEREM, Advanced Manufacturing Institute, King Saud University, Kingdom of Saudi Arabia for financial support. Authors are grateful to all technical staff of Nottingham University, United Kingdom for their assistance in material characterisation. IA and YZ appreciate the cooperation of the University of Mining and Technology, China, for support in hot-press.

References

[1] K. Niihara, New design concept of structural ceramics–ceramics nanocomposites, J. Ceram. Soc. Jpn. 99 (1999) 974–982.
[2] L. Osayande, I. Okoli, Fracture toughness enhancement for alumina system: a review, Int. J. App. Ceram. Technol. 5 (2008) 313–323.
[3] Y. Wu, X. Zhang, J. Guo, Microstructural development and mechanical properties of self-reinforced alumina with CAS addition, J. Eur. Ceram. Soc. 2 (2001) 581–587.
[4] H. Ohnabe, S. Masaki, T. Sasa, Potential application of ceramics matrix composites to aeroengine components, Composites A 30 (1999) 489–496.
[5] P.A. Trusty, J.A. Yeomans, The toughness of alumina with iron: effects of iron distribution on fracture toughness, J. Eur. Ceram. Soc. 17 (1997) 495–504.
[6] S. Maensiri, V. Amornkitbamrung, Carbon nanofiber-reinforced alumina nanocomposite: fabrication and mechanical properties, Mater. Sci. Eng. A477 (2007) 44–50.
[7] N.P. Padture, Multifunctional composites of ceramics and single-walled carbon nanotubes, Adv. Mater. 21 (2009) 1767–1770.
[8] J. Fan, D. Zhao, J. Song, Preparation and microstructure of multi-walled carbon nanotubes toughened Al_2O_3 composite, J. Am. Ceram. Soc. 89 (2006) 750–753.
[9] G. Zhan, J. Kuntz, J. Wan, K. Mukherjee, Single-walled carbon nanotubes as attractive toughing agent in alumina based nanocomposites, Nat. Mater. 2 (2003) 38–42.
[10] I. Ahmad, A. Kennedy, Y.Q. Zhu, Multi-walled carbon nanotubes reinforced Al_2O_3 nanocomposites: mechanical properties and interfacial investigations, Compos. Sci. Technol. 70 (2010) 1199–1206.
[11] F. Inam, T. Pijis, M.J. Reece, The production of advanced fine-grained alumina by carbon nanotubes addition, J. Eur. Ceram. Soc. 31 (2011) 2853–2859.
[12] I. Ahmad, H. Cao, H. Chen, H. Zhao, A. Kennedy, Y.Q. Zhu, Carbon nanotube toughened aluminium oxide nanocomposites, J. Eur. Ceram. Soc. 30 (2009) 865–873.
[13] I. Ahmad, A. Kennedy, Y.Q. Zhu, Wear resistance properties of multi-walled carbon nanotubes reinforced Al_2O_3 nanocomposite, Wear 269 (2010) 71–78.
[14] F. Inam, M.J. Reece, Electrically conductive alumina–carbon nanotubes prepared by spark plasma sintering, J. Eur. Ceram. Soc. 30 (2010) 153–157.
[15] J. Wang, S.Y. Lim, S.C. Ng, L.M. Gan, C.H. Chew, Dramatic effect of a small amount of MgO addition on the sintering of Al_2O_3–5 vol% SiC nanocomposite, Mater. Lett. 33 (1998) 273–277.

[16] Y.K. Jeong, A. Nakahira, K. Niihara, Effects of additives on microstructure and properties of alumina–silicon carbide nanocomposites, J. Am. Ceram. Soc. 82 (1999) 3609–3612.
[17] D.A. Rani, Y. Yoshizawa, K. Hirao, Y. Yamushi, Effect of rare-earth dopants on mechanical properties of alumina, J. Am. Ceram. Soc. 87 (2004) 289–292.
[18] J. Fang, A.M. Thompson, M.P. Harmer, H.M. Chan, Effect of yttrium and lanthanum on the final-stage sintering behavior of ultrahigh-purity alumina, J. Am. Ceram. Soc. 80 (1997) 2005–2012.
[19] S. Lartigue, C. Carry, L. Priester, Grain boundaries in high temperature deformation of yttria and magnesia co-doped alumina, J. Phys. Colloq. 51 (1990) 985–990.
[20] D. Delaunay, A.M. Huntz, P. Lacombe, The Influence of yttrium on the sintering of Al_2O_3, J. Less Common Met. 70 (1980) 115–117.
[21] A.G. Robertson, D.S. Wilkinson, C.H.C. Caceres, Creep and creep fracture in hot-pressed alumina, J. Am. Ceram. Soc. 74 (1991) 915–921.
[22] S. Lartigue, F. Dupau, Grain boundary behavior in superplastic Mg-doped alumina with yttria co-doping, Acta Mater. 42 (1994) 293–302.
[23] F. Cesari, L. Esposito, F.M. Furgiuele, C. Maletta, A. Tucci, Fracture toughness of alumina–zirconia composites, Ceram. Int. 32 (2006) 249–255.
[24] C.E. Borsa, H.S. Ferreira, R.H.G.A. Kiminami, Liquid phase sintering of Al_2O_3/SiC, J. Eur. Ceram. Soc. 19 (1999) 615–621.
[25] M. Ajayan, Nanotubes from carbon, Chem. Rev. 99 (1999) 1787–1799.
[26] T.K. Shen, P. Hing, Ultrasonic through-transmission method of evaluating the modulus of elasticity of Al_2O_3–ZrO_2 composite, J. Mater. Sci. 32 (1997) 6633–6638.
[27] G.R. Anstis, P. Chantikul, D.B. Marshall, A critical evaluation of indentation technique for measuring fracture toughness: I, direct crack method, J. Am. Ceram. Soc. 64 (1981) 533–538.
[28] S. Lartigue-Korineka, C. Carryb, L. Priestera, Multiscale aspects of the influence of yttrium on microstructure, sintering and creep of alumina, J. Eur. Ceram. Soc. 22 (2002) 1525–1541.
[29] R.L. Coble, Diffusion models for hot pressing with surface energy and pressure effects as driving forces, J. Appl. Phys. 41 (1970) 4798–4808.
[30] J.D. Powers, A.M. Glaeser, Grain boundary migration in ceramics, Interface Sci. 6 (1998) 23–39.
[31] C.P.S. Kumar, B. Baron, S. Hampshire, Effect of dopants on densification, microstructure and mechanical properties of alumina–silicon nanocomposites ceramics prepared by pressureless sintering, J. Eur. Ceram. Soc. 24 (2004) 3317–3326.
[32] J.D. Cawley, J.W. Halloran, Dopant distribution in nominally yttrium–doped sapphire, J. Am. Ceram. Soc. 69 (1986) 195–196.
[33] F. Danan, L.Q. Chen, S.P. Chen, Numerical simulation of Zener pinning with growing second-phase particles, J. Am. Ceram. Soc. 81 (1998) 526–532.
[34] S. Sarkar, P.K. Das, Microstructure and physicomechanical properties of pressure-less sintered multi-walled carbon nanotube/alumina nanocomposites, Ceram. Int. 38 (2012) 423–432.
[35] H. Miyazaki, H. Hyuga, K. Hirao, T. Ohji, Comparison of fracture resistance as measured by the indentation fracture method and fracture toughness determined by the single-edge-precracked beam technique using silicon nitrides with different microstructures, J. Euro. Ceram. Soc. 27 (2007) 2347–2354.
[36] B.N. Kim, S. Wakayama, M. Kawahara, Characterization of 2-dimensional crack propagation behaviour simulation and analysis, Int. J. Fract. 75 (1996) 247–259.
[37] A.A. Griffith, Philos. Trans. R. Soc. Lond. 221 (1920) 163.
[38] P. Chantikul, S.J. Bennison, B.R. Lawn, Role of grain size in the strength and *R*-curve performance of alumina, J. Am. Ceram. Soc. 73 (1990) 2419.
[39] T. Nakagawa, I. Sakaguchi, Y. Ikuhara, Yttrium doping effect on oxygen grain boundary diffusion in α-Al_2O_3, Acta Mater. 55 (2007) 6627–6633.
[40] Z.Y. Deng, T. Ohiji, Fracture-mode change in alumina-silicon carbide composites doped with rare–earth impurities, J. Am. Ceram. Soc. 86 (2003) 1789–1792.
[41] W.D. Callister, in: Materials Science and Engineering; An Introduction, 5th ed, John Wiley & Sons, New York, 2000.
[42] J.P. Schaffer, A. Saxena, S.D. Antolovich, T.H. Sanders, S.B. Warner, The Science and Design of Engineering Materials, McGraw-Hill, Chicago, 1995.
[43] E.O. Hall, The deformation and ageing of mild steel: III discussion of results, Proc. Phys. Soc 69 (1951) 747–753.